Investigation of Gravity-Spun, Melt-Spun, and Melt-Blown Polypropylene Fibers Using Atomic Force Microscopy

ANNE DE ROVÈRE, ROBERT L. SHAMBAUGH, EDGAR A. O'REAR

School of Chemical Engineering and Materials Science, University of Oklahoma, Norman, Oklahoma 73019

ABSTRACT: The morphology exhibited in a polymer depends on the particular process and processing conditions used to shape and modify the polymer. This morphology has an important influence on the final polymer product (sheet, molded part, etc.). Ten years ago, atomic force microscopy (AFM) was applied for the first time on polymer materials. Since then, AFM has been used extensively on polypropylene (PP) surfaces, but still very little has been reported on the use of AFM for analyzing PP fibers. The purpose of our work was to show the modifications of (a) the morphology and (b) the microstiffness of PP fiber surfaces processed under different operating conditions. Three fiber production processes were used: gravity spinning, melt spinning, and melt blowing. © 2000 John Wiley & Sons, Inc. J Appl Polym Sci 77: 1921–1937, 2000

Key words: PP fibers; AFM; polymer

INTRODUCTION

Atomic force microscopes (AFMs), also called scanning force microscopes (SFMs), belong to a larger family of instruments—scanning probe microscopes (SPMs)—used as precision tools for the study of material surfaces. The first of these SPMs, the scanning tunneling microscope (STM), was invented in 1981 to study conductive and semiconductive material surfaces.[1] In 1986, piezoelectric rastering was incorporated into the first AFM that could image nonconductive material surfaces with atomic resolution.[2] AFM is a high-resolution tool for studying the morphology, mechanical properties, and viscoelastic properties of material surfaces. The AFM's operating principles are based on measuring the forces (mainly van der Waals forces) that exist between the probe that scans the surface and the surface itself. Atomic resolution can be reached because the

probe's tip that scans over the surface is theoretically constituted by a single atom (it is technically difficult to verify this). Since tip–sample interaction occurs on an atomic scale, structural and conformational details are given on an atomic scale. In 1988, atomic force microscopy (AFM) was applied for the first time on polymer surfaces.[3] AFM images can provide worthwhile information about the polymeric surfaces of films, fibers, and single-crystal polymers.

Surface morphology (thickness and surface roughness) of polymer single crystals was observed by AFM on syndiotactic polypropylene[4] and on polyethylene.[5] Albrecht et al.[6] were among the first to image polymer films and obtain details about fibrillar structures. They examined atactic poly(methyl methacrylate) and found isolated fibrils (5–10 μm wide) arranged in small parallel arrays. Each of the fibrils represented a single polymer chain or a small bundle of a few chains. A spacing of 3.5–5 μm between the fibrils was interpreted as a chain-packing parameter. Snetivy and Vancso[7] obtained a direct visualization of the chain packing by using the AFM technique on uniaxially stretched polyoxymethylene. Their

AFM images revealed microfibrils aligned in the direction of the orientation. The lack of folded polymer chains indicated a high degree of extension of the chains. Side-by-side chain distances were also determined. On mechanically oriented isotatic polypropylene (PP) film, several research teams[8,9] were able to resolve individual methyl groups; this resolution gave information about the methyl group pattern and the alignment, packing, and twisting of PP chains. AFM also has allowed a direct visualization of the helical conformation of syndiotactic PP.[9] This visualization was particularly difficult to obtain since helices are not stabilized by strong interchain forces.

AFM has been used to study a number of natural (cotton and wool) and synthetic fibers. For example, Curtin Carter et al.[10] described an AFM technique that they used for measuring the irregularities on glass textile fibers; the irregularities were attributed to the fiber-extrusion process. Zhong et al.[11] imaged the surface topography of a silica optical fiber using AFM. Vancso[12] reported the application of AFM to commercially gel-spun PE fibers. His results revealed a surface covered by transversely overgrown ribbons. Vancso[12] also studied nylon fibers: The fibers, which were scanned by AFM for 45 min, showed some deformations with a very specific pattern. The microfibrils, originally smooth and continuous, were broken up into fragments and pushed apart from the fibrillar axis direction. Poly(*p*-phenylene terephthalamide) fibers, commercialized by DuPont as Kevlar™, were investigated by AFM to extract roughness parameters which can be useful in improving processing conditions.[13] AFM applied on carbon fibers[14] unveiled extrusion lines along the fiber and "dirt" particles. The concentration of such particles decreases as the fiber strength increases. High magnification permitted the identification of grain-type structures on the fiber.

AFM can also give unique, high-resolution information on the structure of lamellar polymers. Shish-kebab structures were identified on highly oriented, melt-spun films of polyethylene.[15,16] A shish-kebab structure consists of extended-chain crystals (or needle crystals), called *shish,* with folded-chain lamellar overgrowth, called *kebab.*

Details about spherulite structure were obtained using AFM tapping mode phase imaging on poly(hydroxybutyrate-*co*-valerate) (PHB/HV) from the melt.[17] Data regarding the growth process of spherulites on bisphenol-A polycarbonate thin films were collected by Harron et al.[18] with AFM. High-resolution morphology studies of disklike spherulites were also achieved using contact-mode AFM.

Our work described herein presents topographical, structural, and mechanical information about the effects of processing conditions on PP fiber surfaces. The fibers were produced by three methods: gravity spinning, melt spinning, and melt blowing. The surfaces were examined for spherulites. Spherulite diameters and fiber roughness were studied as a function of the fiber size. Spherulite deformation by postdrawing (cold and hot) was also examined. The effects of (a) the die-head temperature and (b) the fiber speed (which depends on the take-up roll speed) on local stiffness were studied for the melt-spinning process.

EXPERIMENTAL

Equipment

Gravity-spinning Equipment

For all experiments, Fina Dypro® PP was used. This polymer had an MFR of 88, an M_w of 165,000, and a polydispersity of 4. The PP pellets were melted at 225°C and pressurized in a 1.905-cm (0.75-in.) diameter Brabender extruder with a 20 : 1 $L : D$ and a 3 : 1 compression ratio. The molten polymer was fed to a spin pack containing a Zenith gear pump. The Zenith pump then metered the polymer to a single hole die head. Refer to Tyagi and Shambaugh[19] for further details on the equipment. The spinning direction was downward (see Fig. 1).

In the gravity-spinning process, the molten polymer stream was allowed to collect upon a horizontal screen placed under the die head; only gravity exerted a force on the exiting polymer. The position of the screen was varied from about $h = 5$ cm to $h = 182$ cm. The gravity force was, of course, much greater for larger h. Two runs were performed with these same operating conditions: a die-head temperature of 320°C, a spin-pack temperature of 310°C, and a polymer flow-rate of 0.34 g/min.

Melt-spinning Equipment

The polymer melt was processed with the same system that was used for gravity-spun fibers. However, in this case, the fibers were collected with either a mechanical take-up roll (for speeds
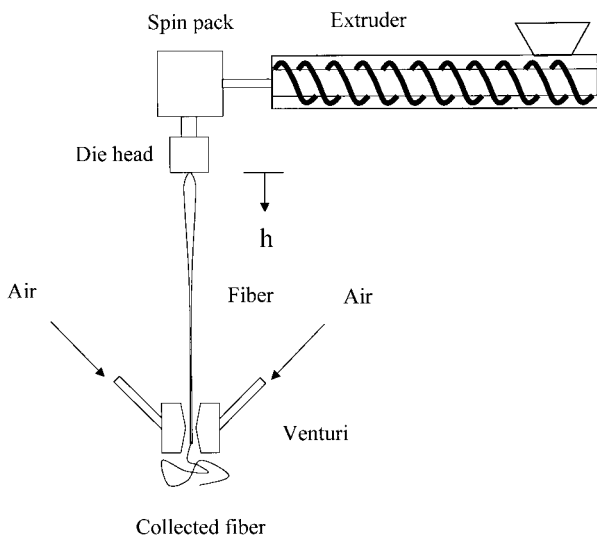
Figure 1 Experimental equipment for melt spinning.

≤ 1000 m/min) or an air-powered venturi device (for speeds > 1000 m/min). Either take-up device applied an additional stress to the fiber stream; as a result, the fiber attenuated more rapidly. The speed of the fiber was controlled by the take-up roll speed or the air velocity in the venturi device. The speed of the fiber was determined from the following continuity equation[20]:

$$v = m/\rho A \qquad (1)$$

where v is the fiber speed; A, the fiber cross-sectional area; m, the polymer mass flowrate; and ρ, the fiber density. The polymer mass flowrate m was determined by collecting and weighing a quantity of fiber over a 1-min-time interval. The diameters of the fibers were determined using an optical microscope with a micrometer eyepiece. All diameter measurements were taken at room temperature, and the fiber density was assumed to be a constant 0.895 g/cm^3.[20] The effects of the die-head temperature and the fiber speed were studied, and the operating conditions used are reported in Table I.

A few melt-spun fibers were also processed using an Instron capillary rheometer as a heating and extruding device. The fibers were drawn and collected on a mechanical take-up roll. The PP pellets were fed manually into the heated extrusion barrel (11.8-mm diameter). When the polymer was melted, a plunger positioned on the top of the barrel jacket was moved down at a monitored speed of 5 mm/min. The motion of the plunger pushed the polymer through a capillary (0.5-mm diameter). At the exit of the capillary, the polymer filament was collected on a mechanical take-up roll that drew the polymer stream into a fine fiber. The fiber threadline was 30 cm long, and the polymer throughput (0.27 g/min) was determined by weighing the fibers over a timed period. The barrel jacket and the capillary were both maintained at 200°C.

Melt-blowing Equipment

The polymer melt was processed with the same extrusion line as the one described for the gravity-spinning process. However, for the melt-blowing process, a melt-blowing (air–polymer) die head was installed on the spin pack.[21] Heated air was provided to the air–polymer die. The drag force of the air caused the melt to elongate rapidly into a fine fiber with a small diameter; this attenuation process is much more rapid than in conventional melt spinning. The fibers were collected on an open, horizontal screen placed at various positions below the die head. The operating conditions are described in Table II.

Table I   Operating Conditions for Melt-spinning Process; Extruder Temperature = 225°C

Die-head Temperature (°C)	Spin-pack Temperature (°C)	Polymer Mass Flowrate (g/min)	Fiber Speed Range (m/min)
251	281	1.09	37,[a]1251–2413
289	281	1.09	52,[a] 462–2481
313	281	1.09	57,[a] 426–2276
343	281	1.09	76,[a] 406–2592

[a] These speeds were produced with gravity spinning; all other speeds were produced with a mechanical take-up roll or a venturi system.

Table II   Operating Conditions for the Melt-blowing Process; Extruder Temperature = 225°C

Die-head Temperature (°C)	Spin-pack Temperature (°C)	Polymer Mass Flowrate (g/min)	Gas-line Heaters (°C)	Run
305	295	1.22	300	1
320	310	0.34	Ambient air	2
320	310	0.34	No air[a]	3

[a] Gravity-spun fibers.

Procedures

Atomic Force Microscopy

AFM images were taken in air using a Nanoscope III System (Digital Instruments, Santa Barbara, CA). The scanning head was a D-type with a Digital Instruments Si_3N_4 force modulation cantilever (225 μm long, 2–3 μm thick, 30 μm wide, spring constant $\sim$ 1–5 N/m). To position the tip close to the surface, the samples were installed on the piezoelectric tube with the aid of an optical microscope connected to a camera. The measurements of material stiffness via AFM sensitivity were carried out using the tapping mode. The same cantilever-tip assembly was used for all the measurements so that comparable values could be obtained. Spherulite characterizations and lamellar characterizations were done from amplitude images obtained using the force-modulation mode. All other data (spherulite diameter and roughness) were determined from height images in the tapping mode.

Fiber-diameter Measurements

The fiber diameters were measured with a Nikon Labophot2 polarizing microscope equipped with a micrometer eyepiece. The eyepiece was calibrated with a scaled objective micrometer.

RESULTS AND DISCUSSION

Structural Analysis by AFM

A structural analysis was performed on the surface of fibers produced with the three processes described earlier (gravity spinning, melt spinning, and melt blowing). Some of the fibers were subjected to a postdrawing step at either ambient or elevated temperature. The effect of this postprocessing was determined via AFM.

Gravity-spinning Process

Using the procedure described above, PP fibers were collected at positions (h values) ranging from 5 to 182 cm below the die head. Two replicate runs were performed with these same operating conditions: T_{dh} (die-head temperature) = 320°C, T_{sp} (spin-pack temperature) = 310°C, and m (polymer mass flowrate) = 0.34 g/min.

Figure 2 shows the attenuation of the fiber diameter as a function of the position h of the collection screen. The two runs produced nearly the same diameter profile. The diameter attenuated to a final plateau diameter of about 100 μm for $h \geq 50$ cm. Figure 3 shows the surface of a gravity-spun fiber imaged with two different modes: Figure 3(a) is a topographic (height) image and Figure 3(b) is a force-modulation mode (amplitude) image. This fiber was collected 22 cm under the die head. The surface of the fiber is entirely covered by spherulites. Spherulites are the most common entities encountered during the solidification of a quiescent semicrystalline polymer melts.[22] The spherulites consist of polycrystalline aggregates formed from a radiating array of crystalline fibrils that branch to create a three-dimensional structure of approximately radial symmetry. Each branch is composed of lamellae (folded polymer chains) and are interconnected by regions of amorphous material.[23] In both Figure 3(a) and Figure 3(b), the spherulites seem randomly distributed over the surface of the fiber. This lack of preferential orientation or alignment of the spherulites along the fiber's axis contrasts with the work of Lee and Li.[24] Lee and Li studied the evolution of crystalline-phase morphology in high molecular weight polyethylene (HMWPE) and observed an alignment of spherulites on drawn HMWPE billets (by die drawing). The difference between Lee and Li's findings and our work may be due to the fact that, in our study, the spherulites crystallized while the fibers were on the collection screen. On the collection screen, the
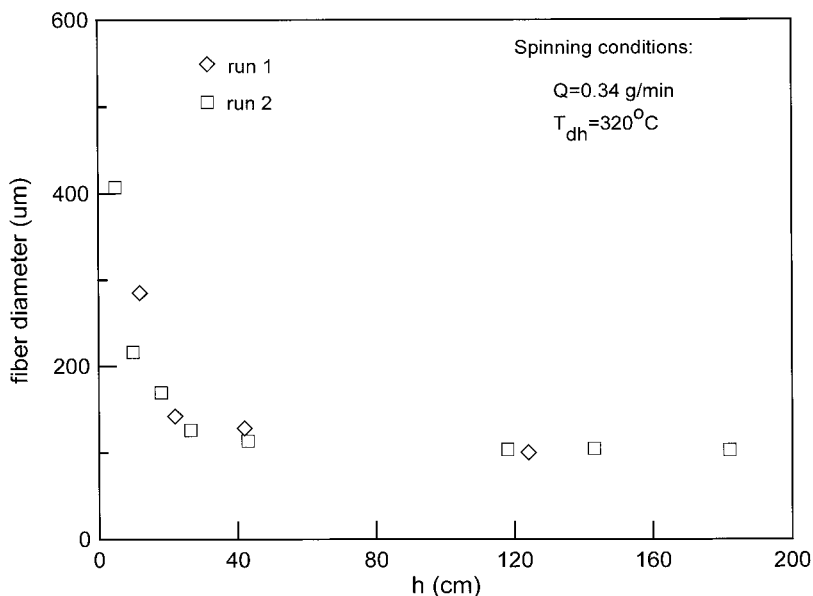
Figure 2 Fiber diameter profile for gravity-spun fibers. Runs 1 and 2 are replicate runs with $T_{dh} = 320°C$ and $Q = 0.34$ g/min. The polymer used was Fina Dypro 88 MFR PP.

fibers are no longer undergoing stress from the gravity force.

The spherulites in Figure 3(a) are edge-to-edge, that is, each spherulite grew until it met the outward growing front of an adjacent spherulite. To analyze in more detail the internal structure of these spherulites, the force-modulation mode was used; Figure 3(b) shows the results of this analysis. As can be seen, force modulation gave a better definition of the spherulite edges and of the radial

arrangement. In Figure 3(b), the edges between spherulites appear as straight lines. Spherulites typically appear this way on SEM and optical micrographs.[25,26]

Figure 4 shows higher magnification images of a gravity-spun fiber; these images show the details of a single spherulite. The left image [Fig. 4(a)] is a topographic view of the inside of the spherulite; the image shows the convex structure of the spherulite. In general, on grav-
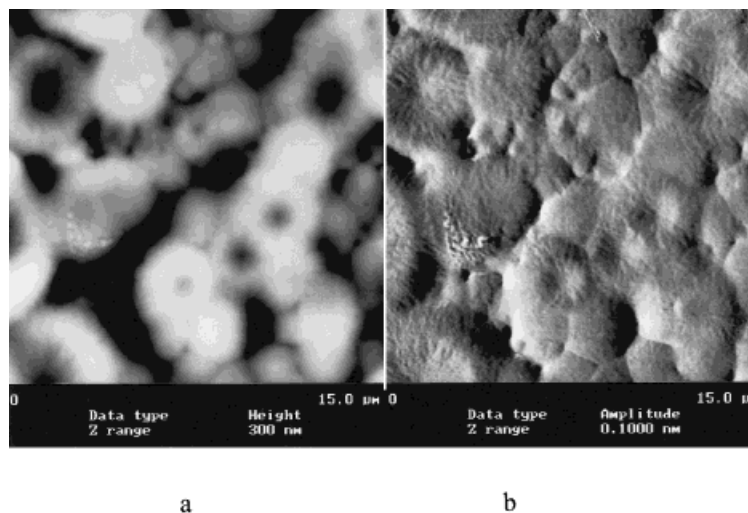

Figure 3 AFM images of spherulitic structure of a gravity-spun fiber collected 22 cm below the die head: (a) topographic image; (b) force modulation mode image.
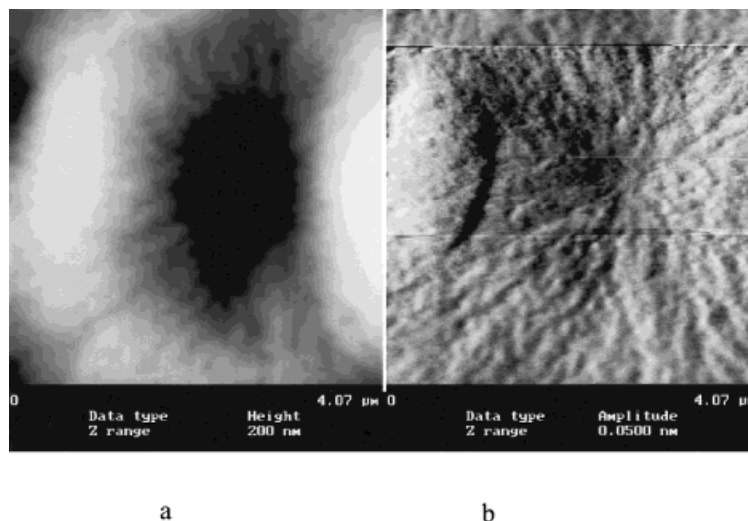
a   b

Figure 4   AFM image of a single spherulite taken with the force modulation mode on a gravity-spun fiber collected 18 cm below the die head: (a) topographic image; (b) force-modulation mode image.

ity-spun fibers, the spherulites we observed were donut-shaped with a perimeter raised in height relative to the surrounding amorphous melt and with a depression at the core of the spherulite. This type of central hole was also observed in polyethylene material.[27] Our finding of a central hole suggests that nucleation does not occur near the surface of the spherulite. Instead, nucleation occurs deep inside the spherulite. Figure 4(b) (a force-modulation image) reveals almost every single chain or bundle of chains. The chains have a typical radial orientation[22] that runs from the center to the edge of the spherulite.

Figure 5 shows the spherulite diameter as a function of h, the collection screen position. The spherulite size decreases for larger h. A spherulite diameter of about 20 μm was found for fibers collected at $h = 12$ cm (an optical microscope was used to measure this large diameter). The diameter decreased to 1.5 μm for fibers collected at $h = 124$ cm.
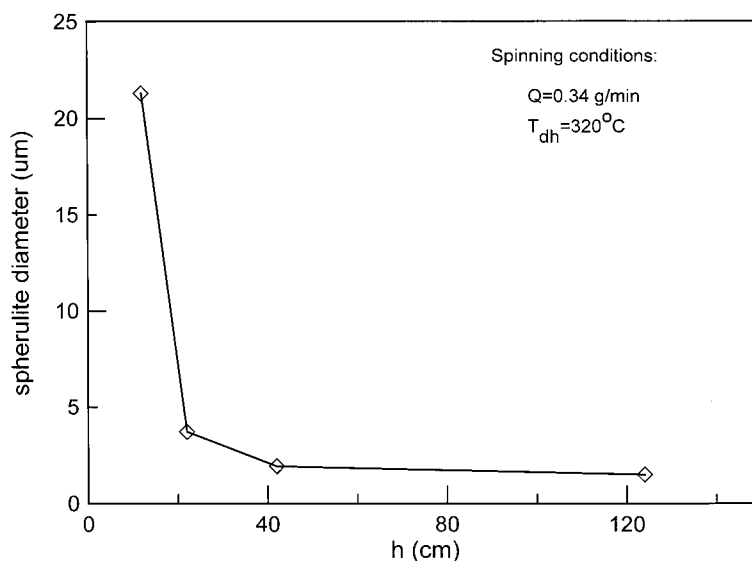

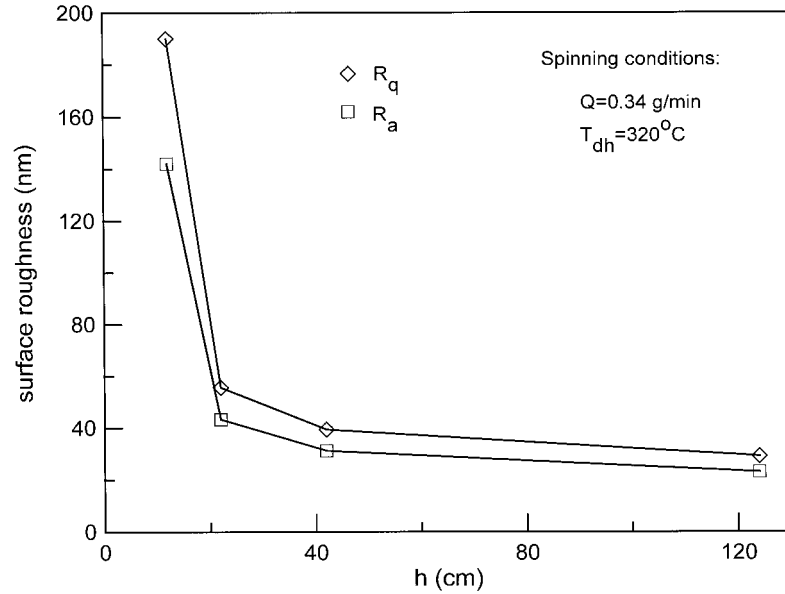**Figure 5**   Spherulite diameter profile for gravity-spun fibers (run 1).

Figure 6 Surface roughness measured by AFM on gravity-spun fibers (run 1).

Figure 6 represents the variation of the fiber roughness as a function of h. The roughness was calculated by mathematically subtracting out the fiber's curvature with the options Planefit and Flatten available in the AFM software. The R_a represents the average roughness of the sample and is defined by the following equation[28]:

$$R_a = \frac{1}{L_x L_y} \int_0^{L_x} \int_0^{L_y} |f(x, y)| \, dxdy \qquad (2)$$

Here, $f(x, y)$ is the surface level relative to the image center plane and L_x and L_y are the dimensions of the surface. The quantity R_q is defined as the highest value of the roughness, that is, the difference between the highest and the lowest features on the surface. The roughness can be determined on a specific area of the AFM image; this area is selected by using a cursor to select a box size. The value of the roughness in the box may vary with the box area. For small box sizes, roughness is small because the box size is of the order of the features (spherulite) size. For large box sizes, the curvature of the fiber contributes to large values of roughness. However, selecting a box size in between the extremes (where roughness values are independent of box size) gives the best measure of roughness. R_a and R_q both exhibit the same decreasing profile. Both roughnesses are high on fibers collected close to the die

head: R_a is about 145 nm and R_q is about 190 nm for fibers collected 12 cm below the die head. In contrast, the roughnesses are relatively low on fine fibers (i.e., fibers collected at large h): R_a and R_q are both about 25 nm on fibers collected 124 cm below the die head. The difference between the average roughness R_a and the maximum roughness R_q is smaller for larger h values. Thus, the roughness is more uniformly distributed over the surface for higher values of h. The roughness is related to the size of the spherulites: The bigger the fiber, the bigger the spherulites, and the larger the roughness. Generally, spherulites with a large diameter had a deeper center hole than that of spherulites with a small diameter. The center hole depth of these larger spherulites and their high rims (with respect to the amorphous surroundings) can explain the high roughness observed for high values of h.

Figure 7 is a plot of spherulite diameter versus fiber circumference for runs 1 and 2. The solid line in Figure 7 represents a linear correlation between the diameter of the spherulites and the circumference of the fiber for the average of runs 1 and 2. Thus, the size of the spherulites is proportional to the size of the fiber. Table III summarizes the characteristics of the linear regressions that fit run 1, run 2, and the average of both runs. In the three cases, the values for the slopes and the intercepts are very close, that is, the relationship between spherulite size and fiber
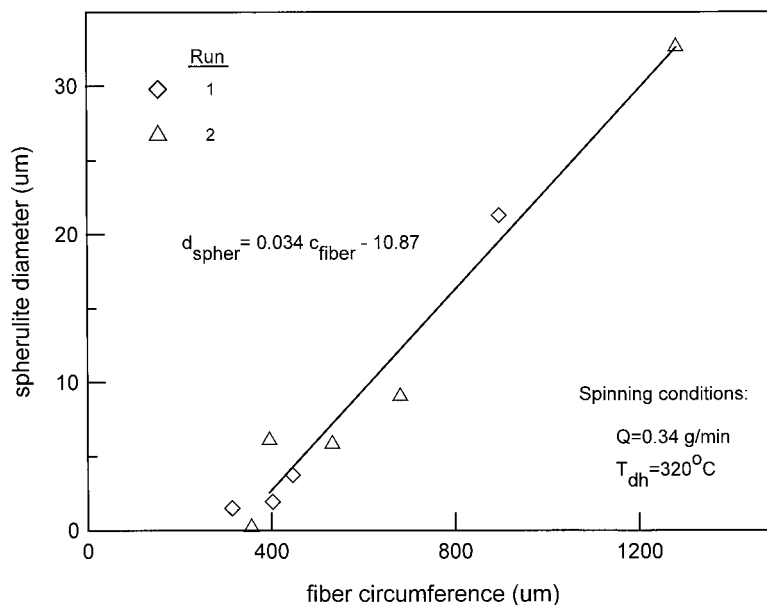
Figure 7 Spherulite diameter versus fiber circumference for gravity-spun fibers.

size is almost the same. For the average of the two runs, the correlation equation can be expressed as

$$d_{\mathrm{spher}} = 0.034 c_{\mathrm{fiber}} - 10.87 \qquad (3)$$

where d_{spher} is the spherulite diameter and c_{fiber} is the fiber circumference. The constant 10.87 is related to the amount of amorphous material surrounding each spherulite. Based on the slope of eq. (3), and assuming a linear alignment of spherulites along the circumference of the fiber, there are about 30 spherulites that can fit along the fiber circumference (for all collection positions). Thus, the number of spherulites on the surface does not vary with the collection screen position. However, the spherulite size depends on the space available for growth. (Smaller diameter fibers cool more rapidly than do fibers of larger diameter. However, for a constant polymer throughput, this cooling effect is balanced by the

rapid transit of the smaller fiber through the cooling zone below the spinneret.[20])

Melt-blowing Process

Melt-blown fibers were processed as described in Table II. The fibers were collected at different positions under the die head, and all the fibers revealed a spherulitic structure when analyzed with the AFM. Figure 8 shows a three-dimensional image of a melt-blown fiber surface covered by spherulites. The image was taken in the tapping mode. The spherulites on these melt-blown fibers present the same characteristics as those of the spherulites on gravity-spun fibers: The spherulite diameter profile decreases with increasing h, and the spherulites are edge-to-edge. Spherulite size was also found to be related to fiber size.

Figure 9 shows the variation of spherulite diameter versus fiber diameter for melt-blown fibers, while Figure 10 shows similar data for both gravity-spun and melt-blown fibers. The equation that resulted from a linear fit of the data is shown on the graph; the r^2 (coefficient of determination) value for the fit is also indicated. As was suggested in the previous section, the intercept is related to the amount of amorphous material and the slope is related to the number of spherulites that can fit along the circumference of the fiber. We assumed the number of spherulites to be equal to the inverse of the slope. If the data of the

Table III Parameters of the Linear Regressions for Gravity-spun Fibers

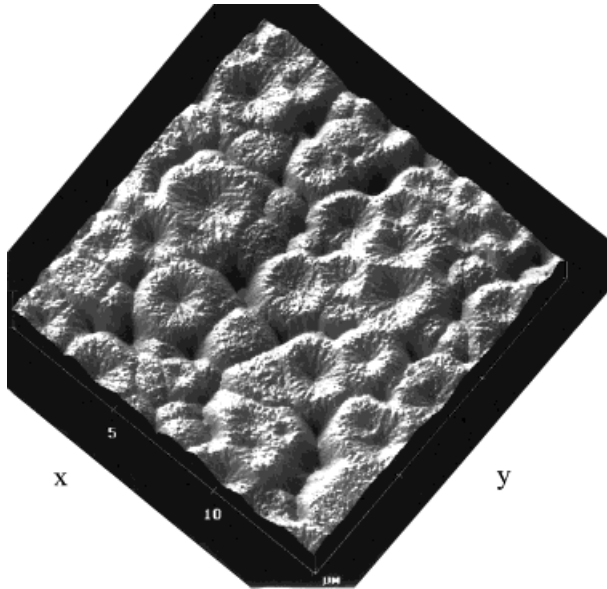|	Run 1	Run 2	Average of Runs 1 and 2
Slope	0.0363	0.0331	0.034
Intercept	−11.549	−10.528	−10.57
r^2	0.9818	0.9623	0.9663

Figure 8   Three-dimensional topographic image of a melt-blown fiber covered by spherulites. The x and y are horizontal coordinates (i.e., in the plane of the fiber surface); the x and y scales are equal and have a magnitude of 5 μm/division. The vertical z scale has a magnitude of 200 nm/division.

two runs are considered separately, about 23 spherulites can fit along the circumference for gravity-spun fibers while only 15 spherulites can fit for melt-blown fibers.

Melt-spinning Process

Melt-spun fibers were processed with the melt-spinning equipment described previously. The operating conditions are summarized in Table I. AFM images produced with the tapping mode and the force-modulation mode did not reveal any spherulites. The stress applied by the take-up roll (or the venturi) probably prevented the formation of spherulites on the surface. Indeed, since spherulitic structures usually grow on nonmoving substrates,[22] it is unlikely that spherulites formed on the melted polymer stream under stress. Because of the length of the threadline (182 cm), the polymer filaments were quite cool when they reached the collection screen.[20] So, even on this nonmoving support, no spherulite can grow. Instead, a shish-kebab structure was observed on the melt-spun fibers. Figure 11 shows an arrangement of close-packed lamellar crystals, identified as shish kebab, on the surface of a melt-spun fiber processed using a venturi to produce a fiber speed of 1500 m/min. A shish-kebab structure was already reported for polybutene-1 ultra-thin films[29] and on polyethylene surfaces.[16] The shish-kebab morphology is a common characteristic of polymer crystallized under strain. Shish-kebab morphology consists of (1) a needle crystalline core (shish) with extended polymer chains and (2) many epitaxial overgrown lamellar crys-
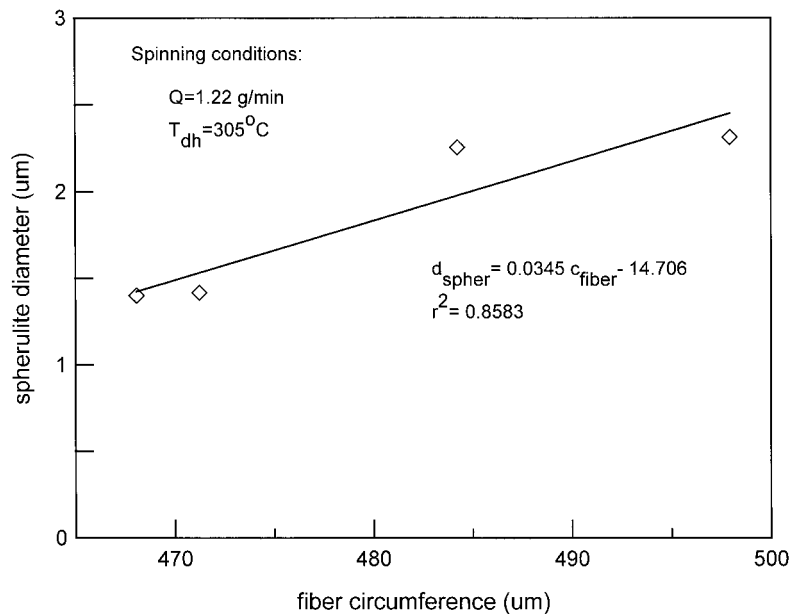

Figure 9   Spherulite diameter versus fiber circumference for melt-blown fibers (run 1).
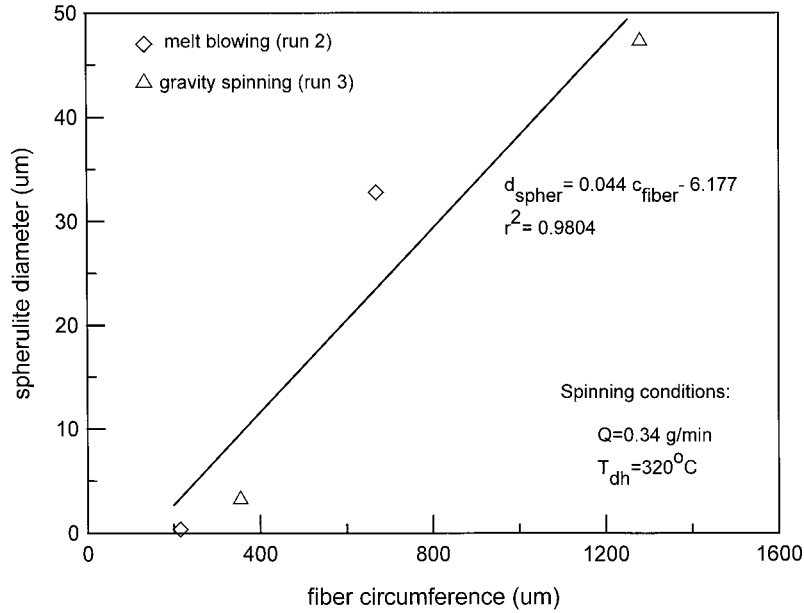
Figure 10 Spherulite diameter versus fiber diameter for melt-blown and gravity-spun fibers.

tals (kebabs) with folded polymer chains surrounded by amorphous materials.[16]

Spherulite Deformation

Two different types of spherulite distributions were observed on the fiber surfaces. The first type was previously described for gravity-spun fibers and melt-blown fibers. The first type consists of edge-to-edge spherulites and contains a very small amount of amorphous material between spherulites (see Fig. 3). The second type of distribution [see Fig. 12(a)] consists of a lower density of spherulites on the surface of the fiber (i.e., there is a larger amount of amorphous material). The second type was observed for fibers processed using a capillary rheometer. Figure 12(a) repre-
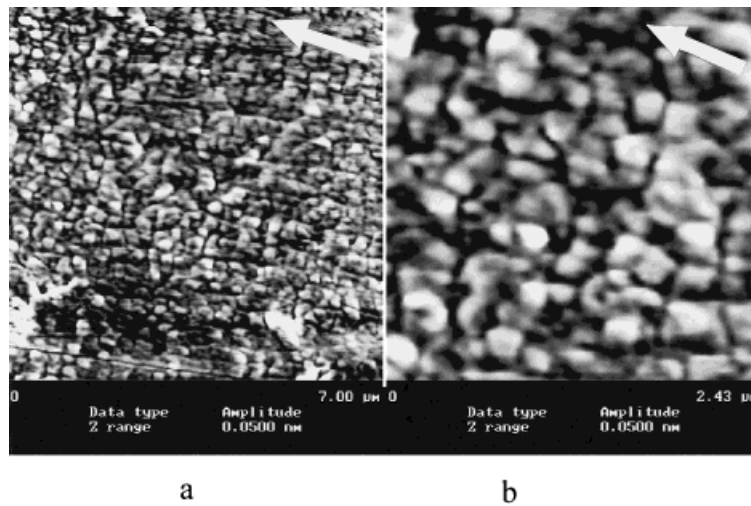

Figure 11 Shish-kebab structure on a melt-spun fiber surface (spun with a venturi at 1500 m/min): (a) force-modulation image with 7-μm scan; (b) force-modulation force image with 2.4-μm scan; the arrows represent the major fiber axis (i.e., the axis in the spinning direction).
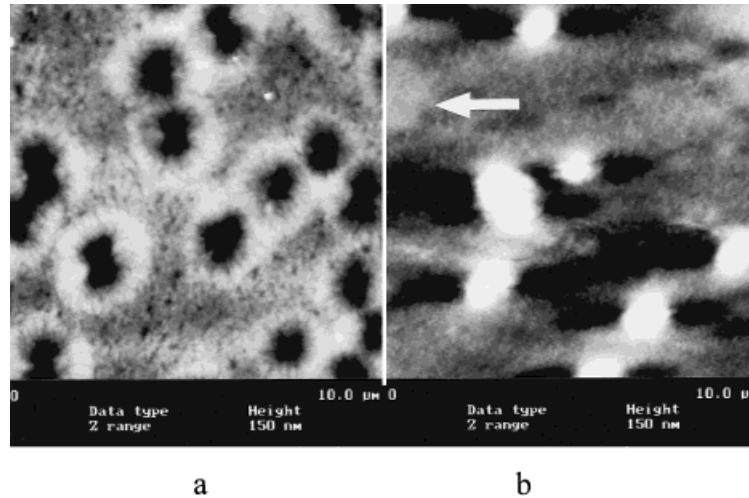
Figure 12 Topographic images of a melt-spun fiber processed with a capillary rheometer: (a) surface before stretching; (b) surface after stretching; the arrow represents the stretch direction.

sents the topography of the surface of a fiber processed with a capillary rheometer. Spherulites appear as isolated units separated by amorphous surroundings. The spherulites have the same shape that was described earlier for gravity-spun and melt-blown fibers, that is, an almost circular shape and a center lower than the rest of the spherulite.

To give a better understanding of the deformation process, the second type of fibers were subjected to postdrawing. Figure 12(b) shows the topography of the surface of a fiber spun from a capillary rheometer. The fiber was postdrawn (elongation less than 3×) at ambient tempera-

ture. The bright spots are apparently the remains of the centers of stretched spherulites. Both Figure 12(a) and Figure 12(b) were imaged under the same conditions (same cantilever, force modulation mode) and their vertical scale (z range) was set at the same level (bright for 0 nm and dark for 250 nm) so that their topographies could be compared. Before deformation, the spherulites had a "crater" shape, a shape which was already described for gravity-spun and melt-blown fibers. The main characteristic of this crater shape is a center depressed with respect to the rest of the spherulite [Fig. 13(a)]. After stretching, the remaining spherulites exhibited a transposed struc-
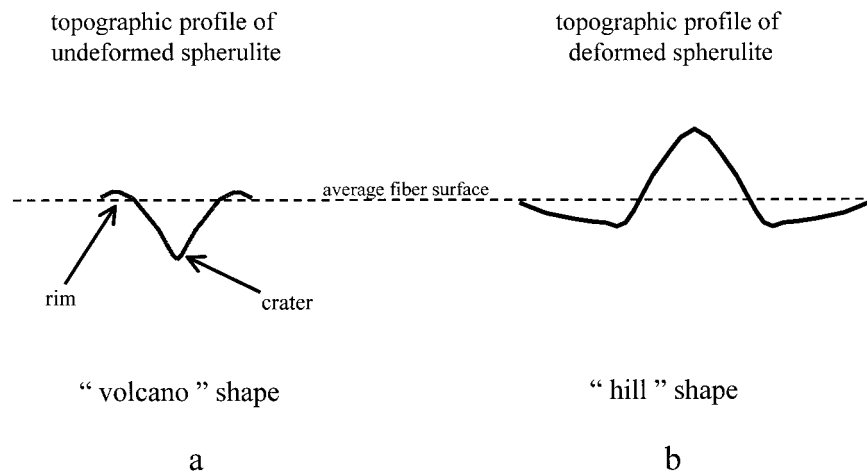

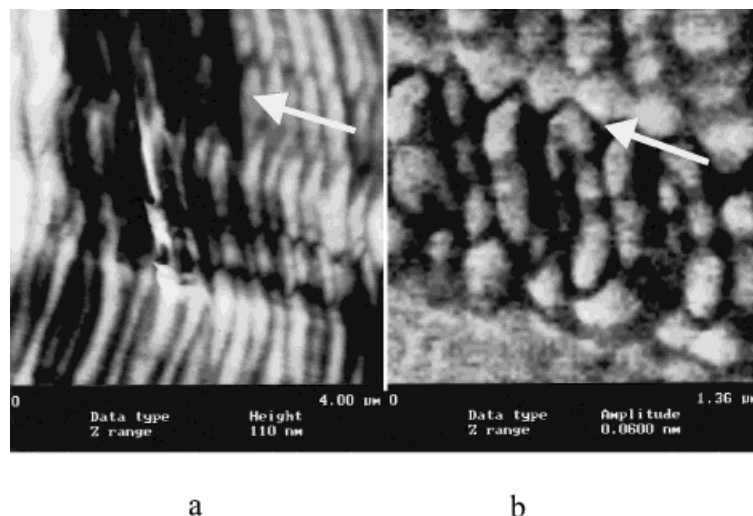**Figure 13** Transformation of spherulite structure from "volcano" shape into "hill" shape.

Figure 14 Lamellar structure on a melt-spun fiber which was processed with a capillary rheometer and poststretched: (a) topographic image of parallel lamellae; (b) image of a lamellar slip; the arrows indicate the direction of stretch.

ture [see Fig. 13(b)]. This structure has a "hill" shape with the center of the stretched spherulite protruding above the rest of the spherulite and the surroundings. In Figure 13(b), the stretching direction is horizontal, and two depressions can be identified on the right and on the left of the deformed spherulites. This can be explained by the particular structure of spherulites and by the fact that the stretching was applied in only one direction. The act of stretching can be decomposed into two mechanisms: (a) elongation of the fiber (i.e., elongation of the spherulites embedded in the fiber) in the direction of the stretching and (b) compression of the fiber diameter and circumference. Both mechanisms result in the deformation of the spherulite from a spherical shape into an ellipsoid.

Lamellar structures were identified on AFM images when additional stress was applied to the fibers (elongation higher than $3\times$) at ambient temperature; this stress leads to the total destruction of the spherulites. Figure 14 shows this
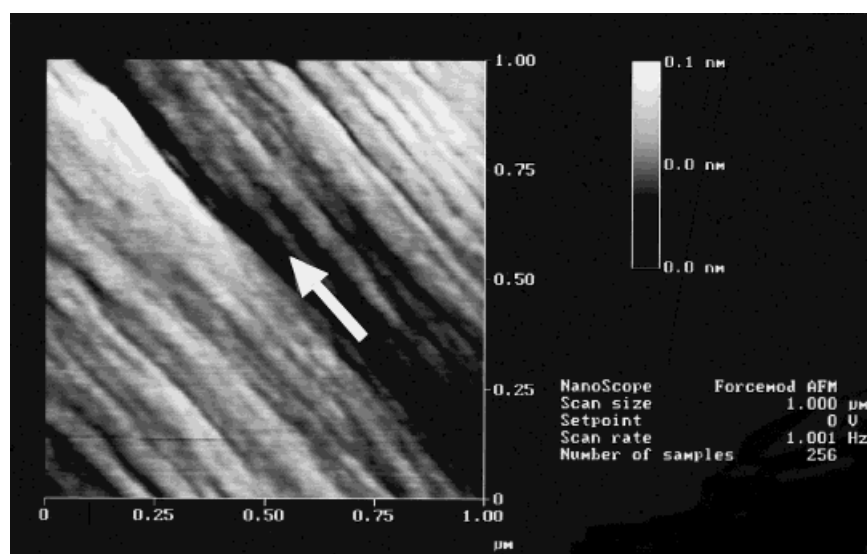

Figure 15 Fibrillar structure on gravity-spun fiber which was postdrawn at 127°C. Force modulation mode was used.
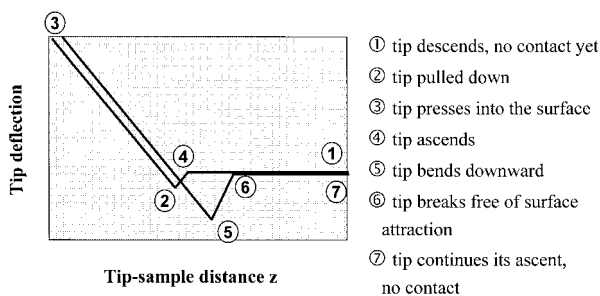
Figure 16 Typical contact-mode force curve.

force plots generated by the AFM. A typical force plot from contact mode AFM is shown in Figure 16. The horizontal axis represents the distance between the tip and the sample. The ascent phase of the probe (positions 1–3) is achieved by moving the sample up. The descent phase (positions 4–7) is achieved by moving the sample down. The cantilever's deflection is plotted on the vertical axis of the graph. When the cantilever bends toward the sample, the slope of the force curve is positive, and when the cantilever bends upward, the slope is negative. The force curve can give information regarding the material elasticity and stiffness. The sensitivity, which is equal to the slope of the force curve while the probe is in contact with the sample surface, is related to the hardness and elasticity of the material. If the material is hard, pressing the cantilever downward will result in a large cantilever deflection (large sensitivity). If the surface is soft, the probe will penetrate the material to a greater extent, and the resulting deflection is smaller (smaller sensitivity). Using the force curve to access material properties at the micron and submicron scale is a unique feature of AFM. Magonov and Reneker[30] showed that the slopes of force curves generated on different materials can be analyzed to compare the hardness and softness of the samples.

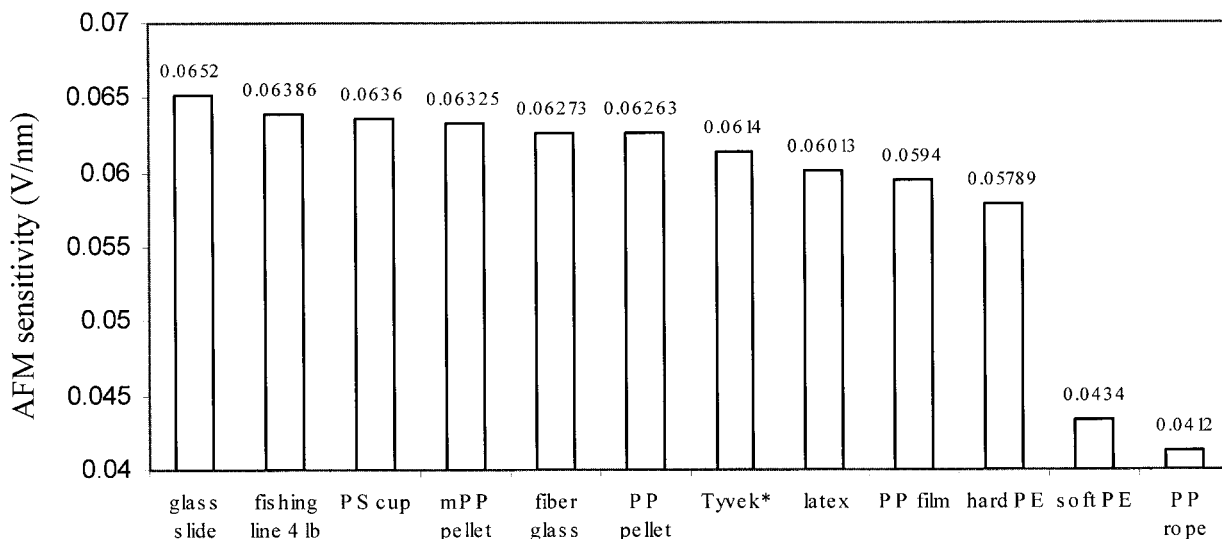With the technique described by Magonov and Reneker, the sensitivity of melt-spun fiber sur-

lamellar structure observed on a melt-spun fiber processed with a capillary rheometer and post-drawn at ambient temperature.

A higher degree of orientation of the molecules was obtained on gravity-spun fibers that were postdrawn at 127°C. This orientation resulted in a fibrillar structure as can be seen in Figure 15.

Stiffness Analysis on Melt-spun Fibers

In addition to the structural analysis that has been presented, a characterization of the nanometer-scale mechanical properties of melt-spun fibers was also performed with AFM. This property evaluation involves (a) measuring the tip-to-sample forces and (b) examining the sample deformation (nanoindentations).[30,31] Our study involved a tip-to-sample force analysis which depended on

Figure 17 AFM sensitivity of different materials: cover glass slide from Corning; monofilament fishing line (4-lb TEST) from DuPont; PS from polystyrene cup; mPP, metallocene PP (27.7 MFR; $M_w = 187,000$; polydispersity = 2.13); PP pellet was FINA Dypro PP pellet (88 MFR); Tyvek® from mailing envelope; latex from gloves; PP film made of FINA Dypro PP; data for hard PE and soft PE from Magonov and Reneker.[30]
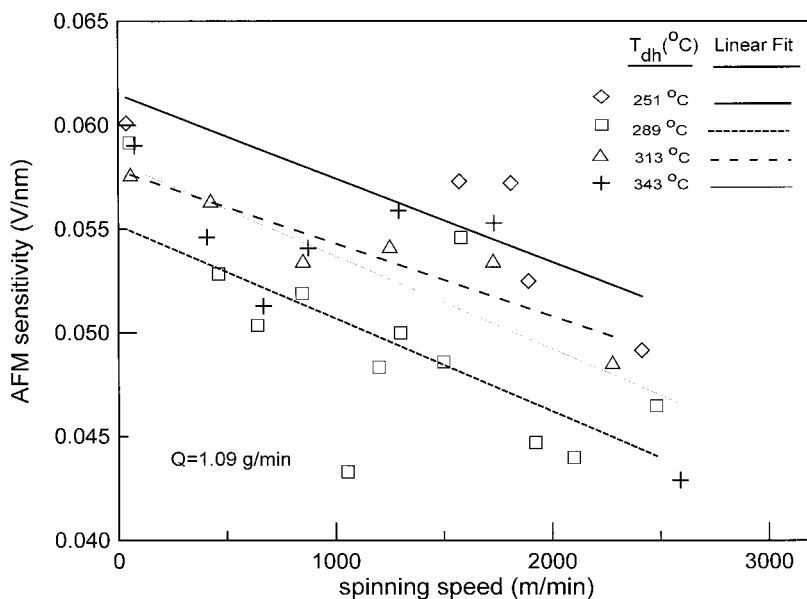
Figure 18   AFM sensitivity versus spinning speed for melt-spinning process.

faces was determined using the tapping mode. The same cantilever-tip assembly was used for all tests so that the sensitivities could be compared. In each case, the force curve plot was generated in a single-step procedure (engaging and withdrawing the tip just once). In addition, other materials were examined in the same way. The slope of the curve was determined from the recorded force plot. Figure 17 gives an example of the range of sensitivity that was obtained with the selected cantilever. The highest sensitivity (0.0652 V/nm) was reached for a glass slide. The lowest sensitivity, 0.0412 V/nm, was obtained by scanning the surface of a commercial PP rope. The sensitivity range is about 0.024 V/nm for the 12 materials tested; the variations are indicative of differences in the microstiffness of the materials.

Measurements were done with a zero-speed cantilever scan over the surface analyzed. Thus, the risk of tip contamination was reduced. In the few cases where the tip seemed contaminated (as evidenced by an unclear image), the cantilever was moved at 2 Hz over the surface of the sample (area 1×1 μm) for a few seconds. This procedure cleared the cantilever tip.

For melt spinning, Figure 18 shows the effect of spinning speed on AFM sensitivity measured on the fiber surface. Data were taken for four different die-head temperatures. For all temperatures, the AFM sensitivity (microstiffness) decreases as the spinning speed increases. To find some possible effect of the die-head temperature

on AFM sensitivity, the fiber speeds were divided into the three speed domains reported in Table IV. The "low-speed" fibers were processed by gravity spinning. The "high-speed" domain corresponds to the highest fiber speed obtained for each die-head temperature. The "medium-speed" domain represents a range of speeds located between the high and low speeds. Figure 19 represents a bar graph of sensitivity as a function of die-head temperature for each of the three speed domains. The sensitivity reported for low speed corresponds to the sensitivity of gravity-spun fibers. The sensitivity reported for high speed corresponds to the sensitivity of high-speed fibers. The sensitivity mentioned for medium speed corresponds to the average sensitivity of fibers spun at speeds greater than the gravity-spun speed

Table IV   Three Fiber-speed Domains for Melt Spinning

Die-head Temperature (°C)	Low Speed[a] (m/min)	Medium Speed (m/min)	High Speed (m/min)
251	37	1251–1504	2413
289	52	462–2134	2481
313	57	426–1728	2276
343	76	406–1732	2592

[a] These low speeds were obtained by gravity spinning; all other speeds were obtained with a mechanical take-up roll or venturi system.
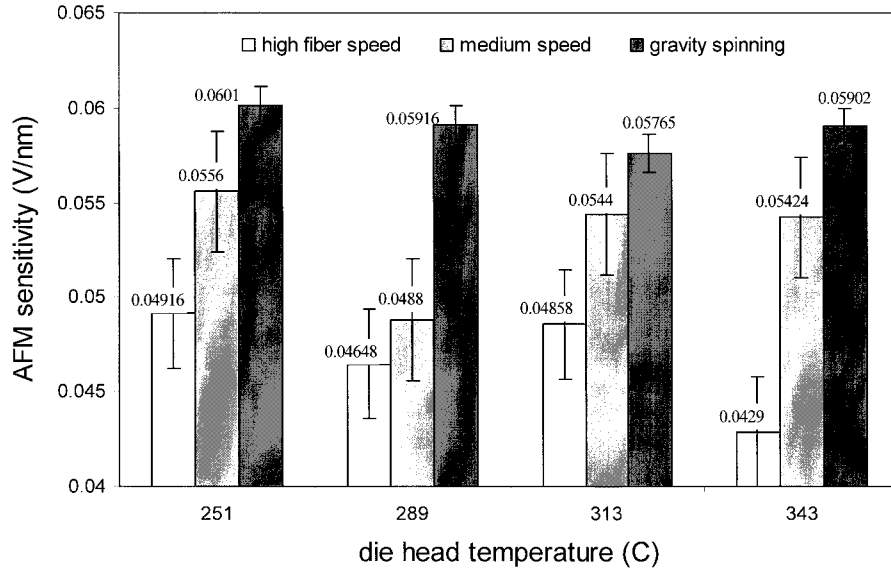
Figure 19 AFM sensitivity versus die-head temperature. The error bars are the standard deviations.

and lower than the highest speed obtained via the venturi. As we mentioned earlier, low-speed fibers exhibit the highest sensitivity for all the die-head temperatures tested. Figure 20 illustrates the variations of AFM sensitivity as a function of the die-head temperature. The lines on the figure are linear fits to the data for each spinning speed range. There appears to be a slight decrease in sensitivity with increasing die-head tempera-

ture. However, this effect is small compared to dependence on the spinning speed.

The AFM sensitivity can be described as a microimpact test in a direction perpendicular to the axis of the fiber. The strength of fibers is known to increase with increased fiber speed, and the AFM sensitivity study shows that the impact resistance of the fiber surface is less for high-speed fibers than for low-speed fibers. This phenomenon
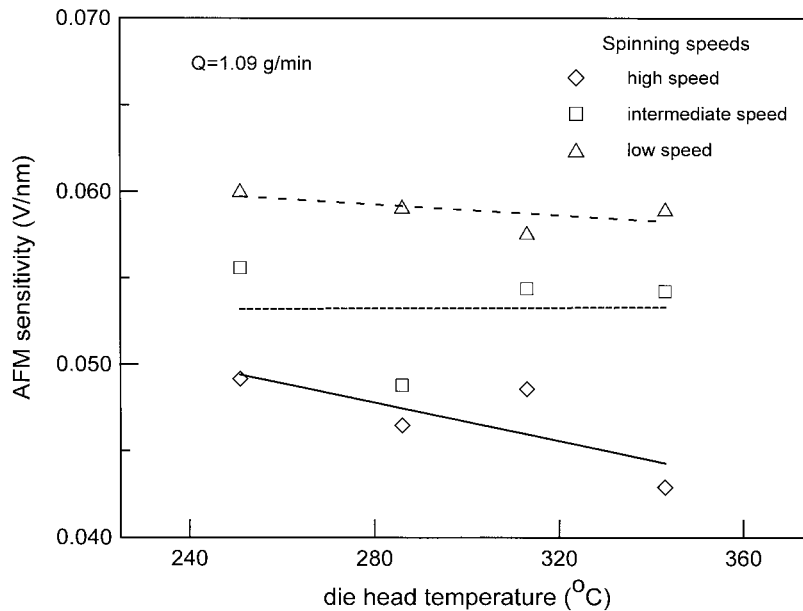

Figure 20 AFM sensitivity versus die-head temperature.

can be explained by considering the structure of the surface. It is possible that the stress applied to high-speed fibers creates surface voids that weaken the surface resistance. Besides, high-speed fibers are usually highly oriented in the direction of the fiber's axis. This orientation is related to the decrease of orientation in all other directions (and, in particular, the decreasing orientation in directions perpendicular to the fiber's axis). It may be possible that, in order to obtain a higher stiffness in the direction of the axis of the fiber, the stiffness perpendicular to the orientation of the fiber has to be sacrificed.

CONCLUSIONS

AFM was applied successfully on PP fiber surfaces to study the effect of processing conditions. Topographic analysis showed many different types of morphologies such as spherulites, shish-kebab, lamellar structures, and fibrillar structures. Spherulites were observed on the surface of gravity-spun and melt-blown fibers. In both processes, the spherulite diameter was proportional to the circumference of the fiber on which the spherulites grew. Spherulite size also varied with the type of process that was used: spherulites were larger on melt-blown fibers than on gravity-spun fibers.

The roughness of gravity-spun fibers and melt-blown fibers was measured. The roughness decreased with decreasing fiber diameter. Shish-kebab structures were observed on melt-spun fiber surfaces.

A mechanical analysis was also performed on melt-spun fibers. This analysis was done using the AFM sensitivity measurement. Thus, this sensitivity was essentially an impact test on a nanometer scale. The sensitivity decreased with increasing fiber speeds or increasing die-head temperatures. The fiber strength is known to increase with increasing fiber speeds. Perhaps the increase of fiber strength in the direction of the axis of the fiber is responsible for the decrease of the fiber resistance in the direction perpendicular to the fiber axis.

NOMENCLATURE

A	fiber cross-sectional area (m^2)
c_{fiber}	circumference of fiber (μm)
d_{spher}	spherulite diameter (μm)
h	position below the spinneret (cm)
m	polymer mass flowrate (g/min)
T_{dh}	die-head temperature (°C)
T_{sp}	spin-pack temperature (°C)
v	fiber speed (m/min)
x	horizontal coordinate in the plane of the fiber surface (y is the other horizontal coordinate)
y	horizontal coordinate in the plane of the fiber surface (x is the other horizontal coordinate)
z	vertical distance above the plane of the fiber surface

Greek Letters

ρ fiber density (g/cm^2)

REFERENCES

1. Schwarzschild, B. Phys Today 1987, 40, 17.
2. Binnig, G.; Quate, C. F.; Gerber, Ch. Phys Rev Lett 1986, 56, 930.
3. Marti, O.; Ribi, H. O.; Drake, B.; Albrecht, T. R.; Quate, C. F.; Hansma, P. K. Science 1988, 239, 50.
4. Tsukruk, V. V.; Reneker, D. H. Macromolecules 1995, 28, 1370.
5. Patil, R.; Reneker, D. H. Polymer 1994, 35, 1909.
6. Albrecht, T. R.; Dovek, M. M.; Lang, C. A.; Grutter, P.; Quate, C. F.; Kuan, S. W. J.; Frank, C. W.; Pease, R. F. W. J Appl Phys 1988, 64, 1178.
7. Snetivy, D.; Vancso, G. J. Macromolecules 1992, 25, 3320.
8. Snetivy, D.; Vancso, G. J. Polymer 1994, 35, 461.
9. Stocker, W.; Schumacher, M.; Graff, S.; Lang, J.; Wittmann, J. C.; Lovinger, A. J.; Lotz, B. Macromolecules 1994, 27, 6948.
10. Curtin Carter, M. M.; McIntyre, N. S.; Davidson, R.; King, H. W. J Vac Sci Technol B 1996, 14.
11. Zhong, Q.; Innis, D.; Kjoller, K.; Elings, V. B. Surf Sci Lett 1993, 290, L688.
12. Vancso, G. J. Am Chem Soc Proceed 1996 ACS Orlando Meeting 1996, 37, 550.
13. Srinivasan, G.; Reneker, D. H. Polym Int 1995, 36, 195.
14. Jangchud, I.; Serrano, A. M.; Eby, R. K.; Meador, M. A. Adv Mater Process 1995, 7, 33.
15. Miles, M. J.; Jandt, K. D.; McMaster, T. J.; Williamson, R. L. Colloids Surf A 1994, 97, 235.

16. Jandt, K. D.; Buhk, M.; Miles, M. J.; Petermann, J. Polymer 1994, 35, 2458.
17. McMaster, T. J.; Hobbs, J. K.; Barham, P. J.; Miles, M. J. Probe Microsc 1997, 1, 43.
18. Harron, H. R.; Pritchard, R. G.; Cope, B. C.; Goddard, D. T. J Polym Sci B 1996, 34, 173.
19. Tyagi, M. K.; Shambaugh, R. L. Ind Eng Chem Res 1995, 34, 656.
20. Bansal, V.; Shambaugh, R. L. Polym Eng Sci 1996, 36, 2785.
21. Uyttendaele, M. A. J.; Shambaugh, R. L. AIChE J 1990, 36, 175.
22. Basset, D. C. Principles of Polymer Morphology; Cambridge University: 1981.
23. Benard, A.; Advani, S. G.; Schultz, J. M. J Polym Sci B 1996, 37, 471.
24. Lee, Y. W.; Li, J. X. J Appl Polym Sci 1993, 48, 2213.
25. Aboulfaraj, M.; Ulrich, B.; Dahoun, A.; G'Sell, C. Polymer 1993, 34, 4817.
26. Al-Raheil, I. A.; Qudah, A. M.; Al-Share, M. J Appl Polym Sci 1998, 67, 1259.
27. Lustiger, A.; Lotz, B.; Duff, T. S. J Polym Sci B 1989, 27, 561.
28. Gould, S. A. C.; Schiraldi, D. A.; Occeli, M. L. Chemtech 1998, Jan., 35.
29. Jandt, K. D.; Mamaster, T. J.; Miles, M. J.; Petermann, J. Macromolecules 1993, 26, 6552.
30. Magonov, S. N.; Reneker, A. H. Annu Rev Mater Sci 1997, 27, 175.
31. Aime, J. P.; Elkaakour, Z.; Odin, C.; Bouhacina, T.; Curely, J.; Dautant, A. J Appl Phys 1994, 76, 754.